



Article

Quantifying Qiyi Glacier Surface Dirtiness Using UAV and Sentinel-2 Imagery

Jiangtao Chen ^{1,2}, Ninglian Wang ^{1,2,3,*} , Yuwei Wu ^{1,2}, Anan Chen ^{1,2}, Chenlie Shi ^{1,2} , Mingjie Zhao ^{1,2} and Longjiang Xie ^{1,2}

¹ Shaanxi Key Laboratory of Earth Surface System and Environmental Carrying Capacity, College of Urban and Environmental Science, Northwest University, Xi'an 710127, China; chenjiangtao@stumail.nwu.edu.cn (J.C.); yuwei.wu@nwu.edu.cn (Y.W.); aachen@nwu.edu.cn (A.C.); max1995@stumail.nwu.edu.cn (C.S.); 202121513@stumail.nwu.edu.cn (M.Z.); longjxie@stumail.nwu.edu.cn (L.X.)

² Institute of Earth Surface System and Hazards, College of Urban and Environmental Sciences, Northwest University, Xi'an 710127, China

³ State Key Laboratory of Tibetan Plateau Earth System, Environment and Resources, Institute of Tibetan Plateau Research, Chinese Academy of Sciences, Beijing 100101, China

* Correspondence: nlwang@nwu.edu.cn

Abstract: The glacier surface is composed not only of ice or snow but also of a heterogeneous mixture of various materials. The presence of light-absorbing impurities darkens the glacier surface, reducing local reflectance and thereby accelerating the glacier melting process. However, our understanding of the spatial distribution of these impurities remains limited, and there is a lack of studies on quantifying the dirty degree of glacier surfaces. During the Sentinel satellite overpass on 21 August 2023, we used an ASD FieldSpec3 spectrometer to measure the reflectance spectra of glacier surfaces with varying degrees of dirtiness on the Qiyi glacier, Qinghai–Tibet Plateau. Using Multiple Endmember Spectral Mixture Analysis (MESMA), the Sentinel imagery was decomposed to generate fraction images of five primary ice surface materials as follows: coarse-grained snow, slightly dirty ice, moderately dirty ice, extremely dirty ice, and debris. Using unmanned aerial vehicle (UAV) imagery with a 0.05 m resolution, the primary ice surface was delineated and utilized as reference data to validate the fraction images. The findings revealed a strong correlation between the fraction images and the reference data ($R^2 \geq 0.66$, $RMSE \leq 0.21$). Based on pixel-based classification from the UAV imagery, approximately 80% of the glacier surface is covered by slightly dirty ice (19.2%), moderately dirty ice (33.3%), extremely dirty ice (26.3%), and debris (1.2%), which significantly contributes to its darkening. Our study demonstrates the effectiveness of using Sentinel imagery in conjunction with MESMA to map the degree of glacier surface dirtiness accurately.

Keywords: dirtiness; light-absorbing impurities; multiple endmember spectral mixture analysis (MESMA); UAV imagery; sentinel-2 data



Citation: Chen, J.; Wang, N.; Wu, Y.; Chen, A.; Shi, C.; Zhao, M.; Xie, L. Quantifying Qiyi Glacier Surface Dirtiness Using UAV and Sentinel-2 Imagery. *Remote Sens.* **2024**, *16*, 3351. <https://doi.org/10.3390/rs16173351>

Academic Editors: Pedro Fidel Espín-López, Massimiliano Barbolini and Andreas J. Dietz

Received: 25 June 2024

Revised: 30 August 2024

Accepted: 4 September 2024

Published: 9 September 2024



Copyright: © 2024 by the authors. Licensee MDPI, Basel, Switzerland. This article is an open access article distributed under the terms and conditions of the Creative Commons Attribution (CC BY) license (<https://creativecommons.org/licenses/by/4.0/>).

1. Introduction

Mountain glaciers, apart from Antarctic and Greenland ice sheets, represent the largest terrestrial ice reservoirs on Earth. In the context of climate change, these glaciers are undergoing accelerated retreat, which has triggered a cascade of issues, including reduced water resource availability [1], increased risk of natural disasters [2], sea level rise [3], and others [4–6]. The surface of glaciers often contains significant amounts of light-absorbing impurities (LAIs) such as black carbon, mineral dust, organic matter, and others [7]. This results in the darkening of the glacier surface, a phenomenon observed in regions such as the European Alps [8,9], the Greenland Ice Sheet [10], and the Qinghai–Tibet Plateau [7]. These LAIs absorb more solar radiation than bare ice, leading to a decrease in surface reflectance, thereby accelerating glacier melting rates and representing positive feedback. Several investigations have been undertaken to analyze the constituents and

concentrations of LAIs in snow, along with their contribution to glacier melting [11]. As many mountain glaciers become snow-free during the summer months, more dark, bare ice is exposed [12]. However, our understanding of the spatial distribution of dark ice remains limited.

In recent years, remote sensing techniques have made great contributions to the study of glacier changes. Unmanned aerial vehicles (UAVs) have demonstrated promising results in glacier surface classification because of their high spatial resolution and reduced susceptibility to cloud interference [9,13]. Naegeli et al. [13] used imaging spectroscopy to analyze the de la Plaine Morte Glacier in the Alps, delineating the abundance of predominant surface materials through spectral angle mapping (SAM). Their investigation revealed a heterogeneous composition of snow, water, debris, and various ice types on the glacier surface. Similarly, Rossini et al. [9] utilized a UAV platform to collect optical and thermal data on the Zebrù Glacier in the Alps. Using support vector machine (SVM) methodology, they classified the primary surface materials of the glacier and assessed the correlation between surface temperature and debris thickness.

While previous studies have successfully classified glacier surfaces [14], distinguishing among snow, clean ice, dirty ice, and debris, they have often lumped dirty ice into a single category, overlooking the nuanced evolution of ice with varying degrees of dirtiness during glacier ablation. Our field measurements reveal significant differences in reflectance among ice types with varying degrees of dirtiness. Therefore, this study categorizes dirty ice into slightly dirty, moderately dirty, and extremely dirty categories, enabling finer classification of glacier surfaces. Building upon prior research [15,16] and field observations, we further augment the classification scheme by incorporating coarse-grained snow and debris.

However, the presence of mixed pixels in remote sensing imagery leads to a decrease in classification accuracy, posing a significant challenge in remote sensing data analysis [17]. Achieving quantification requires moving beyond traditional hard classification methods, as they do not accurately represent true land cover conditions. Multiple Endmember Spectral Mixture Analysis (MESMA), presented by Roberts et al. [18], is a commonly used method for decomposing mixed pixels. It has been applied to studies aiming to classify land cover where a single pixel represents a mixture of materials [19,20]. MESMA assumes that the reflectance of each mixed pixel is a linear combination of spectra from different components or endmembers, with weights representing the abundance of endmembers within the mixed pixel [21]. It has been extensively employed in post-fire burn severity mapping [19,22,23], delineating open-pit coal mining impacts [24], ecosystem monitoring [25,26], and quantifying subpixel urban impervious surfaces [27]. These studies collectively underscore the effectiveness of MESMA in discriminating various land cover types and generating fraction images. However, thus far, the potential of MESMA in mapping the abundance of materials on glacier surfaces remains unexplored. The arduous terrain and harsh environment of mountain glaciers have led to a notable scarcity of in situ reflectance measurements.

This study utilized the ASD (Analytical Spectral Devices) FieldSpec3 spectrometer to measure the reflectance of ice types with varying degrees of dirtiness on the Qiyi glacier, aiming to achieve the following:

- (1) Map the distribution of ice types with varying degrees of dirtiness on glacier surfaces, assess the accuracy of MESMA in simulating the degree of dirtiness on glaciers, and validate the results using UAV imagery.
- (2) Validate the reliability of Sentinel satellite reflectance products using measured reflectance data.
- (3) Provide a reliable approach and method for classifying and monitoring long-term trends in glacier surface dirtiness using remote sensing data.

2. Materials and Methods

2.1. Study Area

The Qiyi glacier ($39^{\circ}14'13''\text{N}$, $97^{\circ}45'18''\text{E}$), located in the northeastern part of the Qinghai–Tibet Plateau (Figure 1), was named after the Chinese glaciologists who first ascended it on 1 July 1958. According to the Second Glacier Inventory [28], the Qiyi glacier is classified as a cirque–valley glacier, covering an area of approximately 2.6 km^2 with a length of about 3.6 km. Glacier accumulation and ablation mainly occur during the summer months. Against the backdrop of global climate warming, its area has decreased annually. The glacier is flanked by relatively high peaks on both sides, with a relatively flat ice tongue and a steep rear wall (Figure 1c,d). Numerous researchers have studied the mass balance [29], equilibrium line altitude [30], surface temperature [15,31], and albedo [32,33], but very few have focused on the degree of surface dirtiness of the Qiyi glacier. A timely and accurate understanding of glacier dirtiness is of great significance for studying glacier mass balance and albedo.

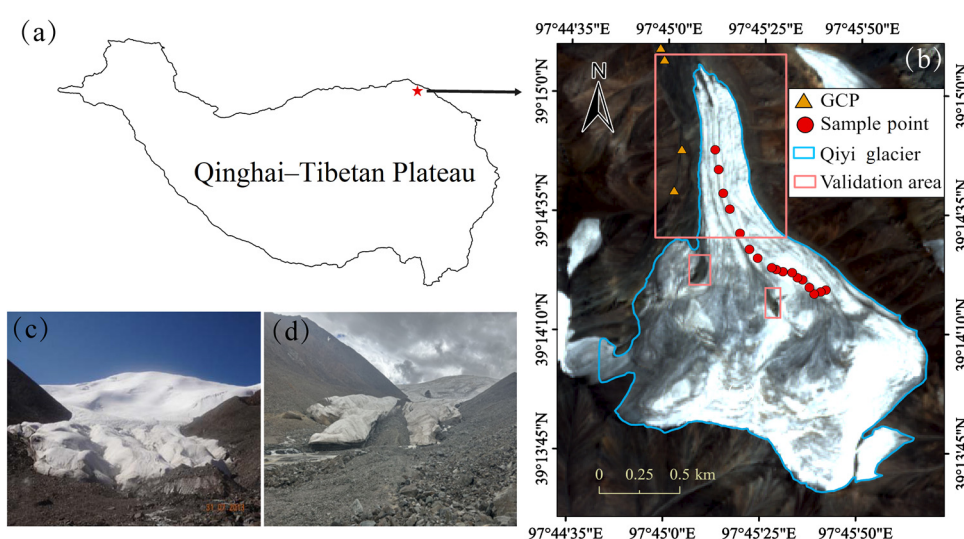


Figure 1. (a) Location of the Qiyi glacier (red star). (b) A true-color RGB image (10 m resolution) of the glacier, with the blue curve outlining its boundary. Red circles represent spectral sampling points, yellow triangles indicate UAV ground control points, and pink rectangles delineate the validation areas. (c,d) are images of the glacier terminus taken on 31 July 2013, and 15 August 2023, respectively.

Through field investigations, it has been observed that during the ablation season, the primary surface materials of the Qiyi glacier include coarse-grained snow, ice with varying degrees of dirtiness (slight, moderate, and extreme), supraglacial rivers, and debris (referring to dark stone blocks exposed because of glacier melting or rolling down from the surrounding mountains). Over the one-month observation period, no deposition of fresh snow was detected, indicating the loss of seasonal snow cover on the glacier.

The Normalized Difference Snow Index (NDSI) [34] was used to delineate the boundary of the Qiyi glacier, with a threshold value of 0.77. Visual interpretation was conducted on UAV imagery to refine the glacier mask used for all subsequent analyses.

2.2. Field Spectroscopy Measurements

The weather during the glacier melting season is highly variable, limiting the opportunities for in situ monitoring. The timing of spectral measurements and the prevailing weather conditions directly influence the quality of data collection. On 21 August 2023, between 11:30 and 13:00 (during the Sentinel satellite overpass), under clear sky conditions, we used an ASD FieldSpec3 spectrometer (with a spectral range of 350–2500 nm and a spectral sampling interval of 1 nm) to measure 56 sample points on the Qiyi glacier. To ensure the representativeness of sampling points and minimize random errors, each observation

session stored 5 spectra with a sampling interval of 1 s. Measurements were conducted with a pistol-grip handle held vertically 1 m above the ice surface, and dark current correction was applied. Spectral measurements were obtained from circular ice surface areas with a diameter of ~50 cm. Spectra of four types of surface materials—coarse-grained snow, slightly dirty ice, moderately dirty ice, and extremely dirty ice—were acquired along the glacier’s longitudinal axis. Safety considerations and instrument operability led to the exclusion of larger supraglacial rivers on the glacier; instead, measurements were taken from supraglacial streams to obtain spectral data.

The removal of abnormal spectral curves and computation of spectral means were conducted using ViewSpecPro 5.6 software. After eliminating erroneous and anomalous spectral curves, a total of 52 spectral curves were finalized. Among these, there were 13 spectral curves for coarse-grained snow, 15 for slightly dirty ice, 14 for moderately dirty ice, 9 for extremely dirty ice, and 1 for a supraglacial river (Figure 2b).

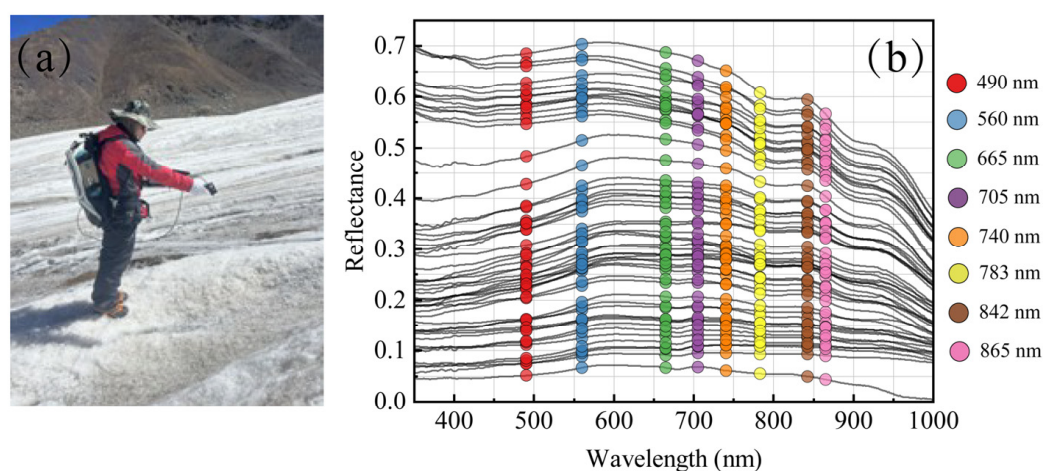


Figure 2. (a) Spectral measurements were collected with a fiber optic probe ~1 m above the ice surface. (b) The actual measured spectral curves are depicted with solid black lines, while colored circles represent the reflectance values at the central wavelengths of Sentinel-2B bands (B2-B8A bands correspond to red to pink hues on the graph).

2.3. UAV and Sentinel-2B Imagery

Utilizing a DJI Matrice 300 RTK UAV equipped with a Zenmuse L1 lens, the visible band spectrum of the Qiyi glacier was acquired. Subsequent post-processing using Pix4Dmapper 4.5.6 professional software yielded a high-resolution (0.05 m) Digital Orthophoto Map (DOM) of the glacier. We pre-defined the flight paths and parameters for the UAV, including a flight altitude of 150 m above ground level, a 60% overlap between images, and an average flight speed of 10 m/s. Because of constraints related to battery life and weather conditions, we conducted four field flights on 15, 17, 19, and 20 August 2023. The UAV acquired a total of 2585 images, of which 45 were subsequently removed because of poor quality after visual inspection.

To ensure accurate geographic registration and minimize errors between the locations of measured spectral points and the spatial positions of UAV data during post-processing, ground control points (GCPs) were strategically deployed on the glacier one day before the UAV flight. The geographic coordinates and elevation of these GCPs were measured and recorded using a Real-Time Kinematic (RTK) device, specifically, the Zhonghaida RTK system. Because of weather conditions and signal constraints, only four GCPs achieved a fixed solution (Figure 1b), while the rest were single-point solutions. Fixed solutions are derived from differential measurements between RTK base and rover stations, providing higher accuracy compared with single-point solutions obtained solely by the rover station. The average errors in the X, Y, and Z directions for the four points are 6 cm, 8 cm, and 14 cm, respectively. This meticulous approach aimed to optimize the accuracy of geographic

registration and minimize discrepancies between measured spectral points and UAV spatial data during subsequent processing phases.

The Sentinel-2B satellite, operated by the European Space Agency (ESA), is a multispectral imaging platform designed for the systematic acquisition of optical imagery over terrestrial and coastal areas at resolutions ranging from 10 m to 60 m. Widely utilized in remote sensing research, it facilitates tasks such as land cover classification, water body monitoring, and snow accumulation detection [35]. In this study, imagery captured by the Sentinel-2B satellite during its pass over the Qiyi glacier on 21 August 2023 was utilized. The imagery data are openly accessible via the ESA's official website (<https://scihub.copernicus.eu> (accessed on 21 August 2023)). Table 1 presents the spectral band names, their respective wavelength ranges, and resolutions used in this study.

Table 1. The spectral band names, corresponding wavelength ranges, and resolutions of the Sentinel utilized in this study.

Band	Range (nm)	Central Wavelength (nm)	Resolution (m)
2 (Blue)	457.5–522.5	490	10
3 (Green)	542.5–577.5	569	10
4 (Red)	650–680	665	10
5 (Vegetation red edge)	697.5–712.5	705	20
6 (Vegetation red edge)	732.5–747.5	740	20
7 (Vegetation red edge)	773–793	783	20
8 (NIR)	784.5–899.5	842	10
8A (NIR narrow band)	855–875	865	20

2.4. Spectral Channel Reflectance Values

Because of hardware limitations of sensor filters, it is impossible for sensors to achieve a 100% response within a predetermined wavelength range. Therefore, satellite sensors often utilize Spectral Response Functions (SRFs) to describe the ratio of the radiance received by the sensor at a given wavelength to the incident radiance. This elucidates the sensor's response intensity across different wavelengths [36]. To achieve spectral matching between field-measured hyperspectral signatures and Sentinel-2B multispectral imagery, given their differing spectral resolutions, spectral integration was performed using the SRF of Sentinel-2B. This process enabled the derivation of channel reflectance values from the field-measured spectra. The SRF can be calculated as follows:

$$R_{rs}(band_i) = \frac{\int_{\lambda_1}^{\lambda_2} R_{rs}(\lambda) SRF(\lambda) d(\lambda)}{\int_{\lambda_1}^{\lambda_2} SRF(\lambda) d(\lambda)} \quad (1)$$

where $R_{rs}(band_i)$ represents the equivalent remote sensing reflectance of band i from the satellite, λ_1 and λ_2 denote the wavelength range of the band, $R_{rs}(\lambda)$ signifies the measured hyperspectral remote sensing reflectance, and $SRF(\lambda)$ stands for the spectral response function at wavelength λ . The computation of ASD-equivalent reflectance using the SRF was performed using Matlab 2023.

The reflectance of different surface materials is shown in Figure 3a, while Figure 3b–f depict corresponding field photographs of these materials.

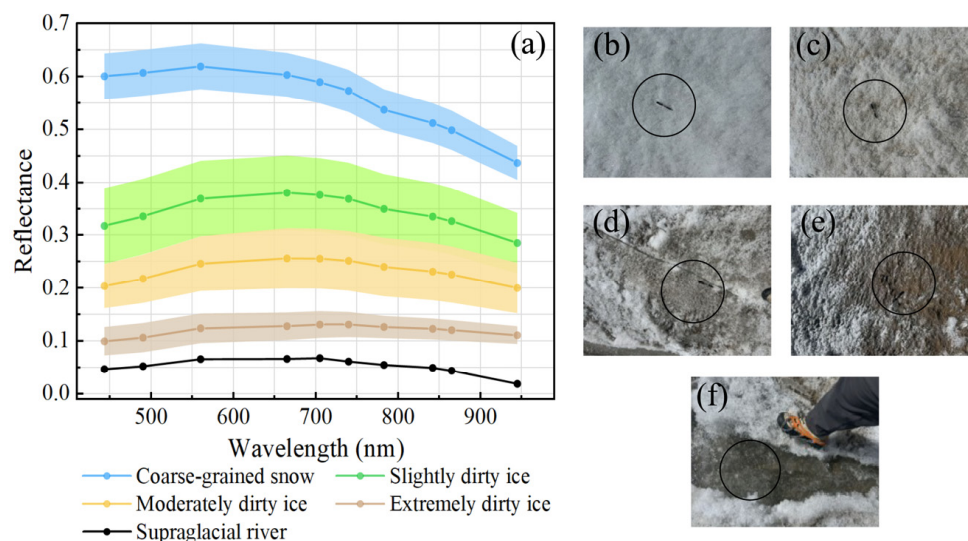


Figure 3. Spectral curves after SRF conversion, where solid lines represent mean values and shaded areas denote standard deviations (a). Photographs of the following categories of ice are shown: (b) coarse-grained snow; (c) slightly dirty ice; (d) moderately dirty ice; (e) extremely dirty ice; and (f) supraglacial rivers. The spectrometer’s field of view is a ~50 cm diameter circle; a pen is placed for scale, aiming to provide readers with a sense of proportion for better comprehension.

The spectral curves of the five glacier surface types, as depicted in Figure 3a, exhibit distinct separability, providing a theoretical basis for the subsequent classification of glacier surfaces. Coarse-grained snow demonstrates higher average reflectance in the visible and near-infrared bands compared with other glacier surface types, with reflectance values exceeding 0.62 ± 0.04 in the red and green bands. The reflectance spectral curves of slightly and moderately dirty ice exhibit consistent fluctuating patterns. Slightly dirty ice attains the highest reflectance values in the red band, reaching up to 0.38 ± 0.07 , while moderately dirty ice similarly achieves maximum reflectance values of 0.25 ± 0.05 in the red band. The presence of impurities in the ice reduces reflectance in the blue and green bands. As dirtiness increases, extremely dirty ice maintains a similar spectral pattern to slightly and moderately dirty ice, but with significantly reduced amplitude, with reflectance values ranging between 0.1 ± 0.02 and 0.13 ± 0.02 .

2.5. Comparison of Different Atmospheric Correction Methods

To mitigate the influence of satellite atmospheric correction processes on the calculation of final surface reflectance of land cover types, it is imperative to validate the atmospheric correction of satellite surface reflectance using synchronous ground-based spectral information (e.g., ASD FieldSpec4, HyperSas) [37]. The objective is to identify products that closely approximate measured reflectance, thereby maximizing the accuracy of subsequent spectral unmixing analyses. Considering the temporal alignment between the measured spectra and Sentinel data, we conducted comparative analyses using Sentinel-2B data acquired on 21 August 2023. Clean and dirty areas were identified within Sentinel imagery (Figure 4), representing coarse-grained snow and dirty ice on the glacier, respectively. The FLAASH atmospheric correction method, based on the MOTRAN radiative transfer model, is integrated into ENVI 5.3 software [38]. Sen2cor serves as a processor for handling and formatting Sentinel-2 Level-2A products, with atmospheric correction conducted using Look-Up Tables (LUTs) generated by the libRadtran radiative transfer computation package [35]. We also compared the reflectance of L1C products, which had not undergone radiometric calibration and atmospheric correction. Because the glacier area is less affected by the atmosphere because of the high altitude, we can more intuitively see the difference between the reflectance of the top atmosphere and the reflectance of the glacier surface.

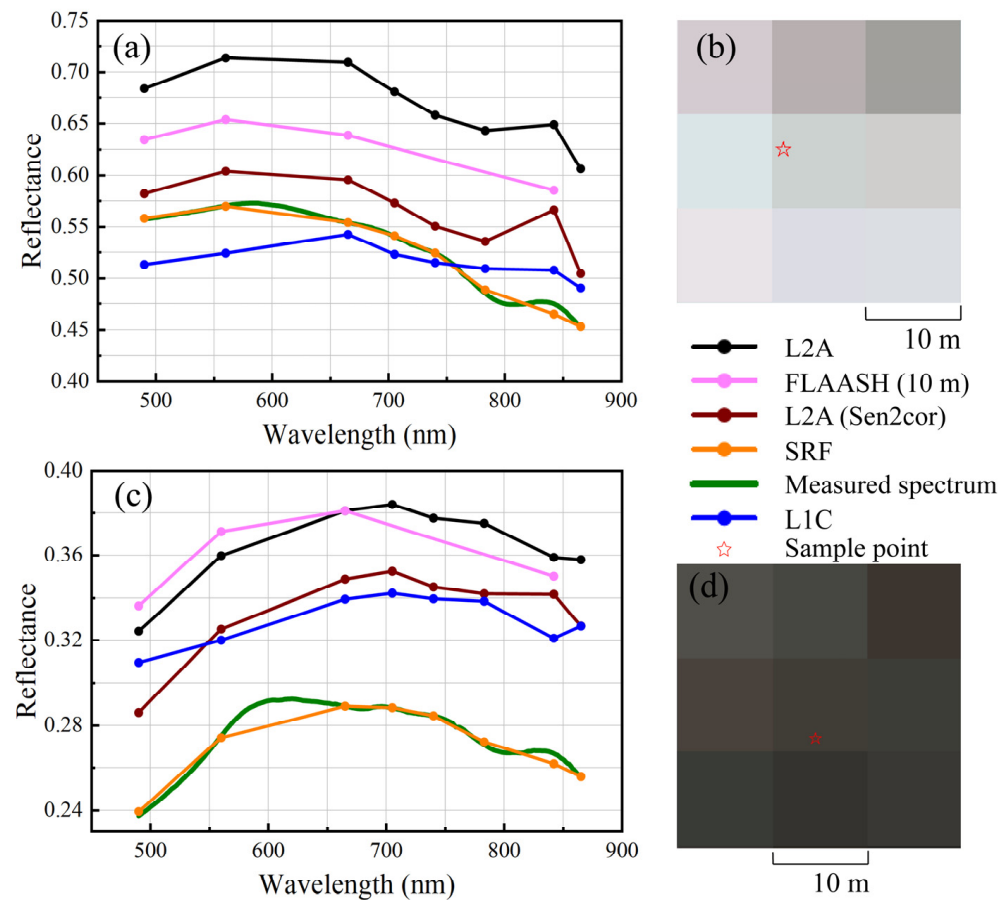


Figure 4. A comparison of measured reflectance and satellite products, where red pentagrams denote the sampling positions of the spectrometer. (a,b) represent relatively clean glacier surfaces, while (c,d) depict relatively dirty glacier surfaces. L2A denotes products produced by the ESA, FLAASH (10 m) signifies atmospheric correction through FLAASH, and L2A (Sen2cor) indicates correction via the Sen2cor plugin. SRF refers to spectral response function conversion, the green line represents the measured spectra, and L1C denotes ESA L1C products.

The Root Mean Square Error (RMSE) was used to assess the differences between the measured values and the three reflectance products. A smaller RMSE indicates higher accuracy in satellite-derived reflectance. RMSE is calculated as follows:

$$RMSE = \sqrt{\frac{\sum_{i=1}^n (y_i - \hat{y}_i)^2}{n}} \quad (2)$$

where n represents the sample size, y_i denotes the measured reflectance value at the i th point, and \hat{y}_i signifies the Sentinel reflectance value at the i th point.

Upon calculation (Table 2), the RMSE values for ESA Level-2A products at the two validation points are 0.149 and 0.094, respectively. Following atmospheric correction through FLAASH, the RMSE values are 0.093 and 0.094, respectively. Moreover, post-correction via the Sen2cor plugin, the RMSE values are 0.050 and 0.064, respectively, indicating minimal errors. Consequently, we opted for Sentinel imagery post-corrected through Sen2cor for our analysis.

Table 2. The RMSE for two validation points.

	L2A	FLAASH (10 m)	L2A (Sen2cor)
Coarse-grained snow	0.149	0.093	0.050
Dirty ice	0.094	0.094	0.064

Notes: L2A refers to ESA Level-2A products; FLAASH (10 m) denotes atmospheric correction through FLAASH; L2A (Sen2cor) signifies correction via the Sen2cor plugin.

2.6. Glacier Surface Classification of UAV Imagery

To match the area covered by ASD sampling points, we resampled the UAV imagery to a resolution of 0.05 m, significantly reducing the computational burden while maintaining classification accuracy. The higher resolution of the orthoimage enabled a finer classification. We manually selected training sets for the following eight predefined ice surface categories: coarse-grained snow, slightly dirty ice, moderately dirty ice, extremely dirty ice, debris, supraglacial rivers, shadows, and bright rocks, with on-site photographs as a reference. Glacier surface classification was conducted using the SVM method. SVM [39,40] is a prominent classification algorithm in machine learning. It discerns a decision hyperplane to separate existing training datasets and subsequently classifies new data based on its position relative to the hyperplane. The effectiveness of SVM as a classifier has been previously demonstrated in the classification of primary materials on glacier surfaces [9,41,42]. More details about the SVM method can be found in [40,42]. Given the limited spectral contrast between the small pixel size of UAV imagery and glacier surface features, which resulted in salt-and-pepper noise [43], a 3×3 median filter was applied to smooth the classification results and mitigate salt-and-pepper noise.

2.7. MESMA Procedure

The MESMA process introduced in this study primarily comprises the following three steps: (1) establishment of a spectral library by incorporating image endmembers as candidate endmembers; (2) optimization of the spectral library by selecting the optimal endmembers to form the final endmember spectral library; and (3) unmixing of Sentinel imagery to obtain fraction images.

2.7.1. Building the Spectral Library

Before applying MESMA, it is essential to define endmembers for decomposing Sentinel imagery. Endmember selection is a crucial step in MESMA, directly impacting the accuracy of spectral representation using a mixed model [24]. Endmember selection involves determining the number of endmembers and their spectral characteristics. Endmembers should exhibit distinguishable attributes within the scene and be of interest to the user [44].

The acquisition of endmembers can be approached through the following avenues: (1) reference endmembers obtained from spectral libraries and (2) image endmembers acquired directly from the image. Reference endmembers, obtainable from field or laboratory sources, offer the advantage of purity. However, their utilization necessitates meticulous image calibration, a process prone to complexities and potential errors due to mismatched pixel sizes [45]. In contrast, image endmembers are readily available and share the same measurement scale as the image data, facilitating consistent calibration during image preprocessing. Therefore, following previous studies [23–25,46], we opted to use image endmembers for spectral library construction. Based on resolution and field surveys, we defined image endmembers as coarse-grained snow, slightly dirty ice, moderately dirty ice, extremely dirty ice, and debris. We used field notes and UAV imagery to identify pure pixels.

2.7.2. Selection of Optimal Endmembers

Upon establishing a spectral library containing candidate image endmembers, the selection of high-quality image endmembers becomes paramount, as it not only reduces computational burden but also enhances MESMA decomposition accuracy [18]. Numer-

ous methods have been developed to optimize spectral libraries. Building upon prior research [19], we utilized the following three metrics to choose the optimal endmembers: (1) Endmember Average RMSE (Root Mean Square Error) (EAR); (2) Minimum Average Spectral Angle (MASA); and (3) Count-based Endmember Selection (CoB). These three metrics are collectively referred to as EMC [46].

EAR assesses the ability of each endmember to model other endmembers within the class by computing the sum of RMSE [47]. EAR can be calculated as follows:

$$EAR_i = \frac{\sum_{j=1}^N RMSE_{i,j}}{n - 1} \quad (3)$$

where i represents the endmember, j denotes the spectral model, N signifies the number of endmembers, and n denotes the number of spectral models. The “ -1 ” is a correction factor to mitigate zero errors resulting from endmember self-modeling.

MASA, like EAR, evaluates the total spectral angle (θ); both metrics do not consider inter-class confusion, focusing solely on intra-class evaluation of endmembers [48]. MASA can be calculated as follows:

$$MASA_i = \frac{\sum_{j=1}^N \theta_{i,j}}{n - 1} \quad (4)$$

The spectral angle (θ) is calculated as follows:

$$\theta = \cos^{-1} \left(\frac{\sum_{\lambda=1}^M \rho_{\lambda} \rho'_{\lambda}}{L_{\rho} L_{\rho'}} \right) \quad (5)$$

where ρ_{λ} represents the reflectance of the endmember, ρ'_{λ} denotes the reflectance of the spectral model, L_{ρ} signifies the length of the endmember vector, and L'_{ρ} indicates the length of the spectral model vector.

The CoB method evaluates the Spectral Match Angle (SMA) of each endmember, assessing its ability to model the number of endmembers in the spectral library successfully, with a defined RMSE threshold to determine success. When applied within endmember classes, this approach is termed InCoB, whereas when applied to endmembers outside of the class, it is termed OutCoB. Optimal endmembers exhibit the highest InCoB and lowest OutCoB, indicating minimal confusion with endmember classes [49].

2.7.3. Spectral Unmixing

The optimized EMC library was applied to MESMA for spectral unmixing of Sentinel imagery. Leveraging the VIPER Tools plugin, spectral unmixing was achieved by coupling two to five endmembers with a shadow endmember [24]. Considering the similarity of dirty ice, we assumed that each pixel in the Sentinel scene could be modeled through a linear combination of one to five ice surface types along with a shadow. By varying the spectral quantity and complexity of the models within the EMC library (ranging from two to six endmembers), iterative processes were conducted. Initially, visually appropriate image sets were selected, followed by the classification of fraction images. In the visual assessment, debris was used as reference points because of its distinct visibility in both UAV imagery and Sentinel imagery, which improved the efficiency and accuracy of visual judgments. Additionally, in cases where the percentage of unmixed pixels was low, new spectra were added to the spectral library to characterize unclassified areas [23]. A threshold of 98% was defined for classified pixels, indicating that the ratio of classified pixels to the total number of pixels in the Sentinel imagery should exceed 0.98. At this point, we considered the MESMA fraction images effective, as too many unclassified pixels would directly affect the accuracy of spectral decomposition and classification outcomes.

Based on previous research [19,23–25], the minimum and maximum allowable fraction values were -0.05 and 1.05 , respectively; the maximum allowable shadow fraction value was 0.8 ; and the maximum allowable RMSE was 0.025 . Finally, to obtain the abundance of non-shadow endmembers for each pixel, the output fraction images were shadow-normalized. The functionalities were implemented using the spectral library plugin VIPER Tools 2.0.

3. Results

3.1. Glacier Surface Classification

In this study, we performed pixel-based classification of the primary materials present on the surfaces of a glacier using UAV imagery. We applied a 3×3 median filter to smooth the classification results and reduce salt-and-pepper effects. The classification results reveal that coarse-grained snow and various degrees of dirty ice dominate the glacier's surface. As depicted in Figure 5, coarse-grained snow and slightly dirty ice are nearly in a 1:1 proportion on the glacier surfaces, accounting for 19.1% and 19.2%, respectively. Moderately dirty ice constitutes the most abundant material on the glacier's surface, occupying one-third (33.3%) of the glacier area. The proportion of extremely dirty ice is 26.3%, exceeding one-fourth of the total area. Debris is concentrated and distributed in small areas, representing 1.2% of the glacier surface. Supraglacial rivers, shadows, and bright rocks exist in small areas on the glacier surface, accounting for 0.1%, 0.5%, and 0.2%, respectively. The pixel-based classification effectively illustrates the distribution patterns of the five primary materials (coarse-grained snow, slightly dirty ice, moderately dirty ice, extremely dirty ice, and debris) on the glacier's surface, highlighting the accuracy of the classification.

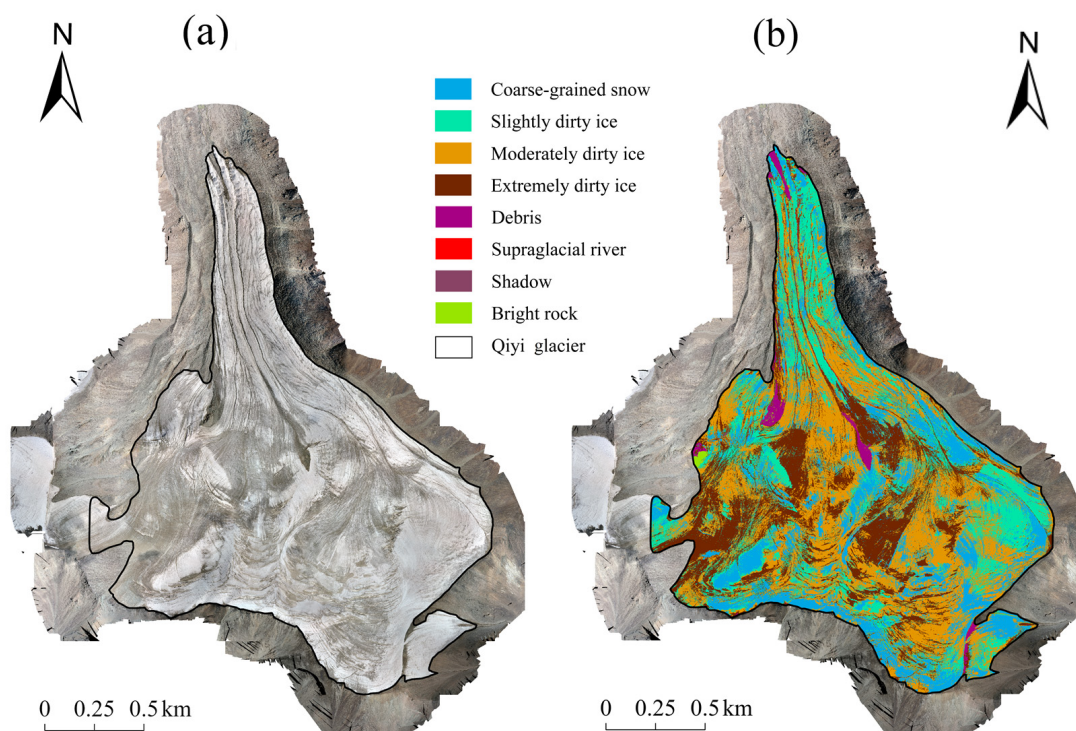


Figure 5. (a) The UAV image and (b) the SVM-classified image.

The central and terminal regions of the glacier exhibit a concentration of debris, clearly discernible in UAV imagery, thus demonstrating the accuracy of UAV-based classification. Additionally, coarse-grained snow and slightly dirty ice are nearly ubiquitous across the entire glacier surface, with a higher prevalence of coarse-grained snow at higher elevations. Conversely, moderately dirty ice and extremely dirty ice are notably concentrated in the

upper regions of the glacier. Bright rocks are mainly concentrated in a small area on the western side of the glacier and at the glacier terminus. Shadows predominantly occur on the western side of the glacier, especially in supraglacial rivers and on the backside of debris, because of the southeast orientation of the sun. Some crevasses appear black under sunlight, potentially causing confusion between shadows and debris in certain areas of the glacier. This confusion is particularly common in supraglacial rivers, where shadows may be misinterpreted as debris because of their darker appearance under sunlight.

A confusion matrix [50] was calculated to validate the accuracy of the classification (Table 3). Utilizing stratified random sampling with equal allocation, 100 accuracy assessment points were randomly generated within each class for visual identification. Validation revealed an overall classification accuracy of 75% with a kappa coefficient of 71%. Notably, the classification accuracy for debris, coarse-grained snow, and slightly dirty ice exceeded 80%, reaching 89%, 88%, and 84%, respectively. Moderately and heavily dirty ice, as well as bright rocks, also achieved an accuracy surpassing 70%, at 76%, 75%, and 72%, respectively. Lower accuracies were achieved in supraglacial rivers and shadows, at 47% and 65%, respectively.

Table 3. The confusion matrix of SVM classification results compared to ground truth data.

Ground Truth Pixels	Classified Pixels							
	Coarse-Grained Snow	Slightly Dirty Ice	Moderately Dirty Ice	Extremely Dirty Ice	Debris	Supraglacial River	Shadows	Bright Rocks
Coarse-grained snow	88	12						
Slightly dirty ice	12	84	4					
Moderately dirty ice	2	20	76	2				
Extremely dirty ice		1	22	75	1	1		
Debris				11	89			
Supraglacial river			10	38	1	47	4	
Shadows			1	26	3	5	65	
Bright rocks				23	5			72

3.2. Optimal Endmembers

As described in Section 3.4, image endmembers were used to build the spectral library. Leveraging field surveys and UAV imagery, candidate endmember spectra of coarse-grained snow, slightly dirty ice, moderately dirty ice, extremely dirty ice, and debris were extracted from Sentinel imagery. The optimization of candidate endmembers was achieved through the utilization of the EAR, MASA, and CoB metrics, resulting in the formation of the final spectral library. This approach not only reduced computational complexity but also enhanced model accuracy.

We finally identified an EMC Library that allowed the MESMA model to decompose 99.2% of pixels in Sentinel imagery successfully. Each class in the EMC library consists of four endmember spectral curves (Figure 6), these five spectral curves represent typical coarse-grained snow, slightly dirty ice, moderately dirty ice, extremely dirty ice, and debris, demonstrating distinct characteristics among different class endmember curves. As depicted in Figure 6, there is a gradual darkening of pixels and a continuous decrease in reflectance from coarse-grained snow to debris. This is accompanied by a reduction in spectral curve amplitudes as the level of dirtiness increases. Reflectance peaks for coarse-grained snow exceed 0.65 at 560 nm; for slightly dirty ice, reflectance generally does not exceed 0.6, with the highest value occurring at 665 nm, whereas for moderately and extremely dirty ice and debris, reflectance exhibits a sharp increasing trend within the 665–705 nm range, with peak values observed at 705 nm.

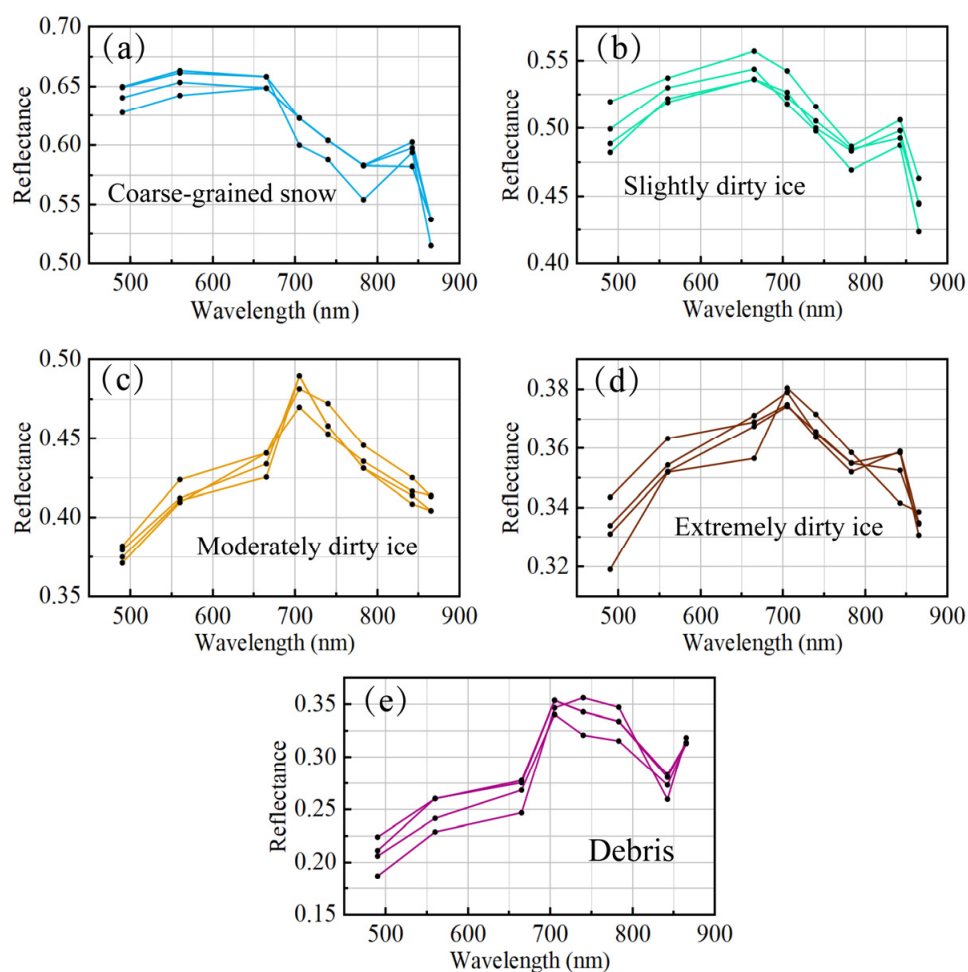


Figure 6. The final spectral endmembers for the following different glacier surface types: (a) coarse-grained snow; (b) slightly dirty ice; (c) moderately dirty ice; (d) extremely dirty ice; and (e) debris.

3.3. Abundance of Glacier Surface Materials

Following the MESMA unmixing of Sentinel imagery, the abundance of five distinct surface materials was quantified for each pixel. We defined thresholds to distinguish among high (0.8–1.0), moderate (0.5–0.8), and low (0.1–0.5); pixels with values below 0.1 were classified as not present (Figure 7).

As depicted in Figure 7, the debris endmember exhibits a highly concentrated distribution pattern, with distinct accumulations observed at the terminus and in the central region of the glacier. These accumulations were not evident in photographs of the glacier taken a decade ago, indicating that over the years, as the glacier melted, debris became exposed, resulting in a gradual darkening of the glacier. Moreover, debris is distributed along the entire boundary of the glacier. Various degrees of dirty ice manifest a dispersed abundance pattern across the glacier, consistent with the findings of the field observations. The coarse-grained snow endmember exhibits relatively low abundance across the central and western regions of the glacier. At higher elevations, the distribution pattern becomes more concentrated, especially in the southeastern part of the glacier. The spatial correspondence with brighter pixels in Sentinel imagery (21 August 2023) further validates the accuracy of MESMA decomposition.

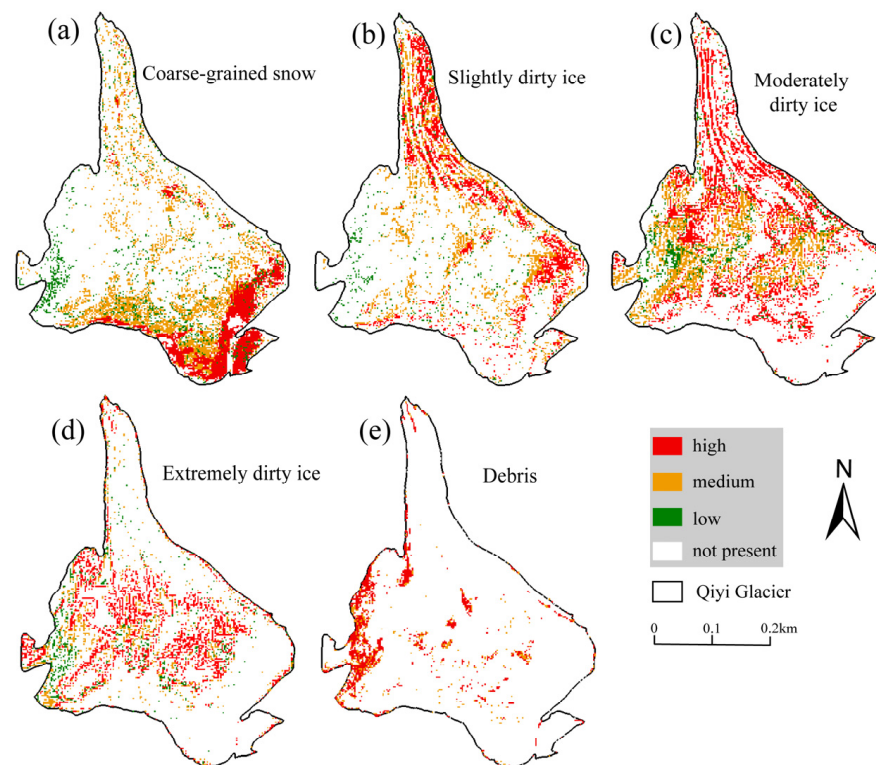


Figure 7. Fraction images for the following five distinct ice surface types are presented: (a) coarse-grained snow; (b) slightly dirty ice; (c) moderately dirty ice; (d) extremely dirty ice; and (e) debris.

Conversely, the extremely dirty ice endmember shows a concentrated distribution with higher abundance in the central glacier regions, presenting a contrasting pattern with coarse-grained snow, where a higher abundance of the latter corresponds to a lower abundance of extremely dirty ice. The slightly dirty ice endmember shows a gradient in abundance from low to high across the glacier, particularly notable in the glacier tongue, where a significant amount of slightly dirty ice is present. The moderately dirty ice endmember tends to distribute along supraglacial rivers in the glacier tongue region, while in the central glacier areas, it shows moderate to high abundance. In the central and western regions of the glacier, confusion between extremely dirty ice and debris is observed because of their accumulation of light-absorbing impurities. This results in comparatively low reflectance, making the area appear darker in Sentinel imagery.

3.4. Accuracy Assessment of MESMA Fraction Images

We used UAV imagery of the glacier tongue and two debris-covered areas (rectangular regions in Figure 1b) to validate the performance of MESMA. UAV imagery of the glacier tongue was acquired the day before the Sentinel satellite overpass, as there was no snowfall during the preceding night, ensuring a relatively stable glacier surface. Therefore, under limited conditions, we consider this dataset to be the optimal choice for validating MESMA. In the glacier tongue section, there is a gradient of ice cover types ranging from low to high abundance, including coarse-grained snow, slightly dirty ice, moderately dirty ice, and extremely dirty ice. However, debris is predominantly found only at the glacier terminus, occurring in limited quantities and with impure pixels. We posit that large debris areas, in the absence of recent snowfall, represent a relatively stable glacier surface in the short term. Therefore, we selected two debris-covered regions in the central part of the glacier for validation. Across the glacier tongue section, we randomly generated 250 validation points on the Sentinel imagery and manually selected 80 points within the two debris-covered areas for validation.

We conducted binary linear regression between the MESMA fraction images and the UAV classification results, calculating R^2 and RMSE. The results, as depicted in Figure 8, show that the accuracy of the debris fraction image is the highest ($R^2 = 0.76$, RMSE = 0.07), followed by moderately dirty ice ($R^2 = 0.71$, RMSE = 0.20). Additionally, coarse-grained snow, slightly dirty ice, and extremely dirty ice achieve R^2 values of 0.69, 0.69, and 0.66, respectively.

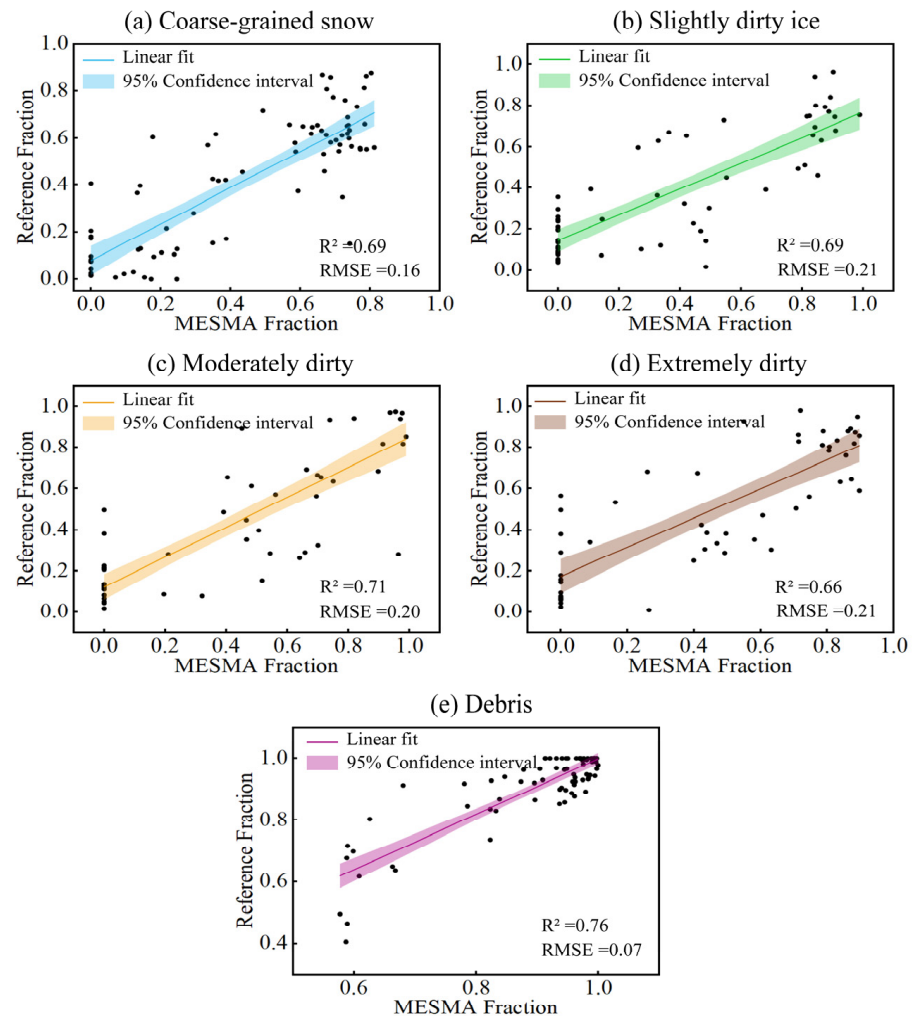


Figure 8. A regression model was constructed to examine the relationship between MESMA fraction images and reference fraction (UAV images). The solid line illustrates the degree of fitting, while the shaded area represents the 95% confidence interval. The determination coefficient (R^2) and root mean square error (RMSE) are presented, $n = 330$.

4. Discussion

4.1. Limitations of UAV Data

Because of constraints imposed by UAV battery life and field conditions, it was not feasible to conduct comprehensive aerial surveys of the entirety of the Qiyi glacier within a single day. However, orthorectified images of the glacier tongue section captured by the UAV were acquired the day before the Sentinel satellite overpass. Given the absence of snowfall on the preceding day, we consider the UAV-derived image to represent a relatively stable glacier surface. It is important to acknowledge that because of glacier dynamics, surface conditions may differ between consecutive days, introducing potential errors during validation. Nevertheless, within the constraints of available data, this dataset represents the optimal choice for validating MESMA. Consequently, validation was limited to the glacier tongue region and two debris-covered areas in the mid-glacier region, while

the accuracy of the unmixing results in the upper glacier remains unknown. Future efforts will focus on obtaining UAV imagery on the day of the satellite overpass to facilitate more precise validation of MESMA fraction images.

The high spatial resolution of UAV imagery enables the SVM algorithm to distinguish different surface materials on the glacier, aligning with previous research findings [9,13]. Satisfactory classification results (user accuracy > 75%) were obtained for the five primary materials on the glacier surface including coarse-grained snow, slightly dirty ice, moderately dirty ice, extremely dirty ice, and debris. However, the classification of supraglacial rivers did not meet satisfactory standards in this study. From the UAV imagery, it is evident that the supraglacial rivers, smoothed and brightened by flowing water, were captured before 12:00 when the sun was positioned in the southeast. These supraglacial rivers flow from south to north, creating natural shadows due to the terrain. Most of these shadows were correctly classified; however, some darker pixels of the supraglacial rivers were misclassified as shadows and debris. The primary confusion occurs between the supraglacial rivers and extremely dirty ice, as the latter is extensively distributed along the supraglacial riverbanks and shares similarly dark pixel values. This misclassification highlights the challenge of accurately distinguishing between these surface types.

Additionally, the oversaturation of some pixels led to the misclassification of coarse-grained snow as supraglacial rivers, highlighting the challenge of delineating shallow water or water body boundaries amidst mixed pixels on bright surfaces [13]. Similarly, during the classification process, confusion between bright rocks and moderately to heavily dirty ice was noted because of similarities in pixel brightness, exacerbated by the prevalence of extensively dirty ice resulting in a salt-and-pepper effect. To mitigate this, a 3×3 median filter and manual adjustments were employed. These adjustments were made to improve the classification accuracy of the UAV imagery, enabling more precise validation of the MESMA unmixing results.

During field measurements, we found that distinguishing between these categories of dirty ice is inherently challenging. Coarse-grained snow can be either clean or dirty, and dirty ice can be either dry or wet. We did not measure the composition and concentration of impurities in the ice, such as various minerals, organic matter, or black carbon, making it challenging to set a definitive threshold to distinguish between coarse-grained snow and ice with varying degrees of dirtiness. Future work will involve measuring the composition and concentration of impurities in the ice to establish thresholds for more accurate classification.

4.2. The Uncertainty of MESMA Procedure

In the MESMA procedure, endmembers can be selected using either field-measured spectra or directly extracted from Sentinel imagery. While field-measured endmembers better meet purity requirements, identifying suitable reference endmembers in high-altitude, harsh glacier environments is challenging. Attempts to find a large, homogeneous flat area on the glacier surface proved difficult because of its heterogeneous and uneven nature, compounded by the presence of flowing liquid water. Although image endmembers might not be as pure, they are easier to obtain and are subjected to the same corrections as other pixels. Consequently, we opted to use image endmembers in this study. Furthermore, the spectral reflectance measured with ASD FieldSpec3 during fieldwork provided valuable information during data processing. This facilitated the differentiation of primary materials on the glacier and offered authentic data for evaluating the reliability of image endmembers.

We found that MESMA can effectively estimate the abundance of different materials on glacier surfaces (coarse-grained snow, slightly dirty ice, moderately dirty ice, extremely dirty ice, and debris), despite some confusion among these surface types. However, the successful application of MESMA critically depends on the selection of pure endmembers and field investigations. Although field measurements can accurately describe ice with varying degrees of dirtiness in the ablation zone, the costs involved are substantial, and long-term observations are challenging. Remote sensing data can be used to study the optical properties of entire glaciers. The Sentinel satellites provide repeat observations every

five days, offering an effective data source for studying daily changes in surface types on glaciers. By utilizing the EMC library and combining it with Sentinel imagery, we can perform mixed pixel decomposition on images throughout the entire ablation period. This process allows us to determine the composition of primary materials on glacier surfaces, ultimately improving our understanding of glacier dirtying processes.

Finally, we found that sub-pixel abundance estimates obtained through MESMA exhibit high accuracy, with low errors (RMSE ranging from 0.07 to 0.21) and high determination coefficients (R^2 ranging from 0.66 to 0.75). These outcomes are consistent with previous studies utilizing MESMA to assess the severity of fire burn scars [23], urban environmental mapping [51], and habitat diversity research [25]. This suggests that MESMA may be suitable for estimating the abundance of surface cover types on the Qiyi glacier. However, further research is needed to confirm its applicability to other glaciers.

4.3. The Prospective Outlook for Future Work

In the context of global warming, many mountain glaciers become snowless in the summer, exposing dirty ice. The light-absorbing impurities in dirty ice cause it to absorb more solar radiation and accelerate the melting process, representing positive feedback. Our work presents the distribution of dirty ice on the glacier surface during the melting stage, which provides a method for more detailed classification of the glacier surface and for analyzing the trend in glacier dirtiness over a long time series. More accurate reflectance is the basis for calculating the mass balance of glaciers. In future work, the reflectance and mass balance of glaciers with different degrees of dirtiness can be further measured by placing a pole on the surface of glaciers with different degrees of dirtiness, thus establishing a relationship between the reflectance and mass balance and, finally, revealing the quantitative impact of glacier dirtiness on the mass balance of glaciers.

5. Conclusions

In this study, the degree of dirtiness on the Qiyi glacier was classified through field surveys and measured spectral curves. Utilizing MESMA on Sentinel images acquired concurrently, we obtained dirtiness classification results. Subsequently, we validated these results using UAV imagery (0.05 m) of the glacier tongue and debris-covered areas. The analysis yielded an R^2 of ≥ 0.66 and an RMSE of ≤ 0.21 , confirming the effectiveness of using Sentinel imagery in conjunction with MESMA to delineate different surface cover types (coarse-grained snow, slightly dirty ice, moderately dirty ice, extremely dirty ice, and debris) on the Qiyi glacier.

Based on the UAV classification results, approximately 80% of the pixels on the Qiyi glacier are covered by slightly dirty ice (19.2%), moderately dirty ice (33.3%), extremely dirty ice (26.3%), and debris (1.2%), indicating a significant presence of dirty materials on the glacier surface, which is a significant factor contributing to the darkening of the glacier. The remaining 19.1% of the glacier surface is covered by coarse-grained snow, while supraglacial rivers, shadows, and bright rocks collectively account for 0.9% of the glacier surface.

Field observation data are essential for validating satellite-derived surface reflectance. By using MESMA, we aim to produce maps that reflect the true surface cover with minimal field sampling effort. The selection of pure endmembers in MESMA is critical, and we believe this approach can be applied to other glaciers as well. The five-day revisit period of Sentinel satellites allows for a deeper understanding of the dirtying processes on glacier surfaces during the ablation season. Our work provides a scientific reference for estimating glacier surface material abundance using Sentinel imagery.

Author Contributions: Conceptualization, J.C., N.W. and Y.W.; methodology, J.C., N.W. and Y.W.; software, J.C., A.C., C.S. and M.Z.; validation, J.C., M.Z. and L.X.; formal analysis, Y.W. and A.C.; investigation, J.C., Y.W., A.C. and L.X.; resources, N.W. and Y.W.; data curation, J.C. and L.X.; writing—original draft preparation, J.C. and Y.W.; writing—review and editing, N.W. and Y.W.; visualization,

L.X.; supervision, A.C.; project administration, Y.W.; funding acquisition, N.W. and Y.W. All authors have read and agreed to the published version of the manuscript.

Funding: This work was supported in part by the National Natural Science Foundation of China under Grants 42130516 and 42171139.

Data Availability Statement: The data presented in this study are available on request from the corresponding author. The data are not publicly available because of privacy restrictions.

Acknowledgments: The authors would like to thank the European Space Agency (ESA) for providing Sentinel images. The authors would like to thank the people who contributed to the collection of in situ data, in particular, Zengkai Zhang and Huidong Liu.

Conflicts of Interest: The authors declare no conflicts of interest.

References

1. Immerzeel, W.W.; Lutz, A.F.; Andrade, M.; Bahl, A.; Biemans, H.; Bolch, T.; Hyde, S.; Brumby, S.; Davies, B.J.; Elmore, A.C.; et al. Importance and vulnerability of the world's water towers. *Nature* **2020**, *577*, 364–369. [[CrossRef](#)] [[PubMed](#)]
2. Terzi, S.; Torresan, S.; Schneiderbauer, S.; Critto, A.; Zebisch, M.; Marcomini, A. Multi-risk assessment in mountain regions: A review of modelling approaches for climate change adaptation. *J. Environ. Manag.* **2019**, *232*, 759–771. [[CrossRef](#)] [[PubMed](#)]
3. Rignot, E.; Mouginot, J.; Scheuchl, B.; van den Broeke, M.; van Wessem, M.J.; Morlighem, M. Four decades of Antarctic Ice Sheet mass balance from 1979–2017. *Proc. Natl. Acad. Sci. USA* **2019**, *116*, 1095–1103. [[CrossRef](#)]
4. Zemp, M.; Huss, M.; Thibert, E.; Eckert, N.; McNabb, R.; Huber, J.; Barandun, M.; Machguth, H.; Nussbaumer, S.U.; Gärtner-Roer, I. Global glacier mass changes and their contributions to sea-level rise from 1961 to 2016. *Nature* **2019**, *568*, 382–386. [[CrossRef](#)]
5. Kaser, G.; Georges, C.; Juen, I.; Mölg, T. Low latitude glaciers: Unique global climate indicators and essential contributors to regional fresh water supply. A conceptual approach. In *Global Change and Mountain Regions: An Overview of Current Knowledge*; Springer: Berlin/Heidelberg, Germany, 2005; pp. 185–195.
6. Lutz, A.F.; Immerzeel, W.W.; Kraaijenbrink, P.D.; Shrestha, A.B.; Bierkens, M.F. Climate change impacts on the upper Indus hydrology: Sources, shifts and extremes. *PLoS ONE* **2016**, *11*, e0165630. [[CrossRef](#)]
7. Cong, Z.Y.; Gao, S.P.; Zhao, W.C.; Wang, X.; Wu, G.M.; Zhang, Y.L.; Kang, S.C.; Liu, Y.Q.; Ji, J.F. Iron oxides in the cryoconite of glaciers on the Tibetan Plateau: Abundance, speciation and implications. *Cryosphere* **2018**, *12*, 3177–3186. [[CrossRef](#)]
8. Dall'Asta, E.; Forlani, G.; Roncella, R.; Santise, M.; Diotri, F.; Morra di Cella, U. Unmanned Aerial Systems and DSM matching for rock glacier monitoring. *ISPRS J. Photogramm. Remote Sens.* **2017**, *127*, 102–114. [[CrossRef](#)]
9. Rossini, M.; Garzonio, R.; Panigada, C.; Tagliabue, G.; Bramati, G.; Vezzoli, G.; Cogliati, S.; Colombo, R.; Di Mauro, B. Mapping Surface Features of an Alpine Glacier through Multispectral and Thermal Drone Surveys. *Remote Sens.* **2023**, *15*, 3429. [[CrossRef](#)]
10. Kraaijenbrink, P.D.A.; Shea, J.M.; Litt, M.; Steiner, J.F.; Treichler, D.; Koch, I.; Immerzeel, W.W. Mapping Surface Temperatures on a Debris-Covered Glacier With an Unmanned Aerial Vehicle. *Front. Earth Sci.* **2018**, *6*, 64. [[CrossRef](#)]
11. Zhang, Y.L.; Gao, T.G.; Kang, S.C.; Sprenger, M.; Tao, S.; Du, W.T.; Yang, J.H.; Wang, F.T.; Meng, W.J. Effects of black carbon and mineral dust on glacial melting on the Muz Taw glacier, Central Asia. *Sci. Total Environ.* **2020**, *740*, 15. [[CrossRef](#)]
12. Hartl, L.; Felbauer, L.; Schwaizer, G.; Fischer, A. Small-scale spatial variability in bare-ice reflectance at Jamtalferner, Austria. *Cryosphere* **2020**, *14*, 4063–4081. [[CrossRef](#)]
13. Naegeli, K.; Damm, A.; Huss, M.; Schaepman, M.; Hoelzle, M. Imaging spectroscopy to assess the composition of ice surface materials and their impact on glacier mass balance. *Remote Sens. Environ.* **2015**, *168*, 388–402. [[CrossRef](#)]
14. Florath, J.; Keller, S.; Staub, G.; Weinmann, M. Optical Remote Sensing for Glacier Monitoring with Respect to Different Snow and Ice Types: A Case Study for the Southern Patagonian Icefield. In Proceedings of the 2021 11th Workshop on Hyperspectral Imaging and Signal Processing: Evolution in Remote Sensing (WHISPERS), Amsterdam, The Netherlands, 24–26 March 2021; pp. 1–5.
15. Wu, Y.; Wang, N.; He, J.; Jiang, X. Estimating mountain glacier surface temperatures from Landsat-ETM + thermal infrared data: A case study of Qiyi glacier, China. *Remote Sens. Environ.* **2015**, *163*, 286–295. [[CrossRef](#)]
16. Hori, M.; Aoki, T.; Tanikawa, T.; Motoyoshi, H.; Hachikubo, A.; Sugiura, K.; Yasunari, T.J.; Eide, H.; Stordvold, R.; Nakajima, Y.; et al. In-situ measured spectral directional emissivity of snow and ice in the 8–14 μm atmospheric window. *Remote Sens. Environ.* **2006**, *100*, 486–502. [[CrossRef](#)]
17. Dietz, A.J.; Kuenzer, C.; Gessner, U.; Dech, S. Remote sensing of snow—A review of available methods. *Int. J. Remote Sens.* **2011**, *33*, 4094–4134. [[CrossRef](#)]
18. Roberts, D.A.; Gardner, M.; Church, R.; Ustin, S.; Scheer, G.; Green, R.O. Mapping Chaparral in the Santa Monica Mountains Using Multiple Endmember Spectral Mixture Models. *Remote Sens. Environ.* **1998**, *65*, 267–279. [[CrossRef](#)]
19. Quintano, C.; Fernández-Manso, A.; Roberts, D.A. Multiple Endmember Spectral Mixture Analysis (MESMA) to map burn severity levels from Landsat images in Mediterranean countries. *Remote Sens. Environ.* **2013**, *136*, 76–88. [[CrossRef](#)]
20. Borsoi, R.A.; Imbiriba, T.; Bermudez, J.C.M.; Richard, C. Deep Generative Models for Library Augmentation in Multiple Endmember Spectral Mixture Analysis. *IEEE Geosci. Remote Sens. Lett.* **2021**, *18*, 1831–1835. [[CrossRef](#)]

21. Roberts, D.A.; Smith, M.O.; Adams, J.B. Green vegetation, nonphotosynthetic vegetation, and soils in AVIRIS data. *Remote Sens. Environ.* **1993**, *44*, 255–269. [[CrossRef](#)]
22. Robichaud, P.R.; Lewis, S.A.; Laes, D.Y.M.; Hudak, A.T.; Kokaly, R.F.; Zamudio, J.A. Postfire soil burn severity mapping with hyperspectral image unmixing. *Remote Sens. Environ.* **2007**, *108*, 467–480. [[CrossRef](#)]
23. Quintano, C.; Fernandez-Manso, A.; Roberts, D.A. Burn severity mapping from Landsat MESMA fraction images and Land Surface Temperature. *Remote Sens. Environ.* **2017**, *190*, 83–95. [[CrossRef](#)]
24. Fernández-Manso, A.; Quintano, C.; Roberts, D. Evaluation of potential of multiple endmember spectral mixture analysis (MESMA) for surface coal mining affected area mapping in different world forest ecosystems. *Remote Sens. Environ.* **2012**, *127*, 181–193. [[CrossRef](#)]
25. Fernández-García, V.; Marcos, E.; Fernández-Guisuraga, J.M.; Fernández-Manso, A.; Quintano, C.; Suárez-Seoane, S.; Calvo, L. Multiple Endmember Spectral Mixture Analysis (MESMA) Applied to the Study of Habitat Diversity in the Fine-Grained Landscapes of the Cantabrian Mountains. *Remote Sens.* **2021**, *13*, 979. [[CrossRef](#)]
26. Cunnick, H.; Ramage, J.M.; Magness, D.; Peters, S.C. Mapping Fractional Vegetation Coverage across Wetland Classes of Sub-Arctic Peatlands Using Combined Partial Least Squares Regression and Multiple Endmember Spectral Unmixing. *Remote Sens.* **2023**, *15*, 1440. [[CrossRef](#)]
27. Wu, C.; Deng, C.; Jia, X. Spatially Constrained Multiple Endmember Spectral Mixture Analysis for Quantifying Subpixel Urban Impervious Surfaces. *IEEE J. Sel. Top. Appl. Earth Obs. Remote Sens.* **2014**, *7*, 1976–1984. [[CrossRef](#)]
28. Guo, W.Q.; Liu, S.Y.; Xu, L.; Wu, L.Z.; Shangguan, D.H.; Yao, X.J.; Wei, J.F.; Bao, W.J.; Yu, P.C.; Liu, Q.; et al. The second Chinese glacier inventory: Data, methods and results. *J. Glaciol.* **2015**, *61*, 357–372. [[CrossRef](#)]
29. Jiang, X.; Wang, N.L.; He, J.Q.; Wu, X.B.; Song, G.J. A distributed surface energy and mass balance model and its application to a mountain glacier in China. *Chin. Sci. Bull.* **2010**, *55*, 2079–2087. [[CrossRef](#)]
30. Wang, N.L.; He, J.Q.; Pu, J.C.; Jiang, X.; Jing, Z.F. Variations in equilibrium line altitude of the Qiyi Glacier, Qilian Mountains, over the past 50 years. *Chin. Sci. Bull.* **2010**, *55*, 3810–3817. [[CrossRef](#)]
31. Wu, Y.; Wang, N.; Li, Z.; Chen, A.; Guo, Z.; Qie, Y. The effect of thermal radiation from surrounding terrain on glacier surface temperatures retrieved from remote sensing data: A case study from Qiyi Glacier, China. *Remote Sens. Environ.* **2019**, *231*, 111267. [[CrossRef](#)]
32. Zhang, Y.L.; Gao, T.G.; Kang, S.C.; Shangguan, D.H.; Luo, X. Albedo reduction as an important driver for glacier melting in Tibetan Plateau and its surrounding areas. *Earth-Sci. Rev.* **2021**, *220*, 11. [[CrossRef](#)]
33. Zhang, T.; Gao, T.; Diao, W.; Zhang, Y. Snow/ice albedo variation and its impact on glacier mass balance in the Qilian Mountains. *J. Glaciol. Geocryol.* **2021**, *43*, 145–157.
34. Riggs, G.A.; Hall, D.K.; Salomonson, V.V. A snow index for the Landsat Thematic Mapper and Moderate Resolution Imaging Spectroradiometer. In Proceedings of the IGARSS '94—1994 IEEE International Geoscience and Remote Sensing Symposium, Pasadena, CA, USA, 8–12 August 1994; Volume 4, pp. 1942–1944.
35. Main-Knorn, M.; Pflug, B.; Debaecker, V.; Louis, J. Calibration and Validation Plan for the L2A Processor and Products of the sentinel-2 Mission. *ISPRS Arch.* **2015**, *40*, 1249–1255. [[CrossRef](#)]
36. Otazu, X.; González-Audiciana, M.; Fors, O.; Núñez, J. Introduction of sensor spectral response into image fusion methods. application to wavelet-based methods. *IEEE Trans. Geosci. Remote Sens.* **2005**, *43*, 2376–2385. [[CrossRef](#)]
37. Sola, I.; García-Martín, A.; Sardonís-Pozo, L.; Álvarez-Mozos, J.; Pérez-Cabello, F.; González-Audiciana, M.; Montorio Llovería, R. Assessment of atmospheric correction methods for Sentinel-2 images in Mediterranean landscapes. *Int. J. Appl. Earth Obs. Geoinf.* **2018**, *73*, 63–76. [[CrossRef](#)]
38. Zhang, C.; Liu, S.; Liu, Y.; Pei, X. The Application and Evaluation of Spectral Reconstruction of Hyperion Based on Radiative Transfer Model. *Remote Sens. Land Resour.* **2010**, *22*, 30–34.
39. Cortes, C.; Vapnik, V. Support-vector networks. *Mach. Learn.* **1995**, *20*, 273–297. [[CrossRef](#)]
40. Burges, C.J. A tutorial on support vector machines for pattern recognition. *Data Min. Knowl. Discov.* **1998**, *2*, 121–167. [[CrossRef](#)]
41. Di Mauro, B.; Baccolo, G.; Garzonio, R.; Giardino, C.; Massabò, D.; Piazzalunga, A.; Rossini, M.; Colombo, R. Impact of impurities and cryoconite on the optical properties of the Morteratsch Glacier (Swiss Alps). *Cryosphere* **2017**, *11*, 2393–2409. [[CrossRef](#)]
42. Zhu, L.; Xiao, P.; Feng, X.; Zhang, X.; Wang, Z.; Jiang, L. Support vector machine-based decision tree for snow cover extraction in mountain areas using high spatial resolution remote sensing image. *J. Appl. Remote Sens.* **2014**, *8*, 084698. [[CrossRef](#)]
43. Kraaijenbrink, P.D.A.; Shea, J.M.; Pellicciotti, F.; Jong, S.M.d.; Immerzeel, W.W. Object-based analysis of unmanned aerial vehicle imagery to map and characterise surface features on a debris-covered glacier. *Remote Sens. Environ.* **2016**, *186*, 581–595. [[CrossRef](#)]
44. Quintano, C.; Fernández-Manso, A.; Shimabukuro, Y.E.; Pereira, G. Spectral unmixing. *Int. J. Remote Sens.* **2012**, *33*, 5307–5340. [[CrossRef](#)]
45. Drake, N.A.; Mackin, S.; Settle, J.J. Mapping Vegetation, Soils, and Geology in Semiarid Shrublands Using Spectral Matching and Mixture Modeling of SWIR AVIRIS Imagery. *Remote Sens. Environ.* **1999**, *68*, 12–25. [[CrossRef](#)]
46. Tane, Z.; Roberts, D.; Veraverbeke, S.; Casas, Á.; Ramirez, C.; Ustin, S. Evaluating Endmember and Band Selection Techniques for Multiple Endmember Spectral Mixture Analysis using Post-Fire Imaging Spectroscopy. *Remote Sens.* **2018**, *10*, 389. [[CrossRef](#)]
47. Dennison, P.E.; Roberts, D.A. Endmember selection for multiple endmember spectral mixture analysis using endmember average RMSE. *Remote Sens. Environ.* **2003**, *87*, 123–135. [[CrossRef](#)]

48. Dennison, P.E.; Halligan, K.Q.; Roberts, D.A. A comparison of error metrics and constraints for multiple endmember spectral mixture analysis and spectral angle mapper. *Remote Sens. Environ.* **2004**, *93*, 359–367. [[CrossRef](#)]
49. Roberts, D.A.; Dennison, P.E.; Gardner, M.E.; Hetzel, Y.; Ustin, S.L.; Lee, C.T. Evaluation of the potential of Hyperion for fire danger assessment by comparison to the Airborne Visible/Infrared Imaging Spectrometer. *IEEE Trans. Geosci. Remote Sens.* **2003**, *41*, 1297–1310. [[CrossRef](#)]
50. Foody, G.M. Status of land cover classification accuracy assessment. *Remote Sens. Environ.* **2002**, *80*, 185–201. [[CrossRef](#)]
51. Phinn, S.; Stanford, M.; Scarth, P.; Murray, A.T.; Shyy, P.T. Monitoring the composition of urban environments based on the vegetation-impervious surface-soil (VIS) model by subpixel analysis techniques. *Int. J. Remote Sens.* **2002**, *23*, 4131–4153. [[CrossRef](#)]

Disclaimer/Publisher’s Note: The statements, opinions and data contained in all publications are solely those of the individual author(s) and contributor(s) and not of MDPI and/or the editor(s). MDPI and/or the editor(s) disclaim responsibility for any injury to people or property resulting from any ideas, methods, instructions or products referred to in the content.